Extremely large magnetoresistance and electronic structure of TmSb

Yi-Yan Wang,[1] Hongyun Zhang,[2] Xiao-Qin Lu,[1] Lin-Lin Sun,[1] Sheng Xu,[1] Zhong-Yi Lu,[1] Kai Liu,[1] Shuyun Zhou,[2,3] and Tian-Long Xia[1,*]

[1]*Department of Physics and Beijing Key Laboratory of Opto-electronic Functional Materials & Micro-nano Devices, Renmin University of China, Beijing 100872, People's Republic of China*

[2]*State Key Laboratory of Low Dimensional Quantum Physics and Department of Physics, Tsinghua University, Beijing 100084, People's Republic of China*

[3]*Collaborative Innovation Center of Quantum Matter, Beijing 100084, People's Republic of China*

(Received 11 November 2017; published 23 February 2018)

We report the magnetotransport properties and the electronic structure of TmSb. TmSb exhibits extremely large transverse magnetoresistance and Shubnikov-de Haas (SdH) oscillation at low temperature and high magnetic field. Interestingly, the split of Fermi surfaces induced by the nonsymmetric spin-orbit interaction has been observed from SdH oscillation. The analysis of the angle-dependent SdH oscillation illustrates the contribution of each Fermi surface to the conductivity. The electronic structure revealed by angle-resolved photoemission spectroscopy (ARPES) and first-principles calculations demonstrates a gap at the X point and the absence of band inversion. Combined with the trivial Berry phase extracted from SdH oscillation and the nearly equal concentrations of electron and hole from Hall measurements, it is suggested that TmSb is a topologically trivial semimetal and the observed XMR originates from the electron-hole compensation and high mobility.

DOI: 10.1103/PhysRevB.97.085137

I. INTRODUCTION

Recently, rare earth monopnictides LnX (Ln=La, Y, Ce, Nd and X=Sb, Bi) have drawn much attention and been studied widely [1–27]. In these materials, extremely large magnetoresistance (XMR) is a remarkable signature since conventional nonmagnetic metals usually show a small magnetoresistance (MR) of only a few percent. XMR has also been observed in several other materials such as WTe_2 [28–30] and (Nb/Ta)As_2 [31–35]. Several mechanisms have been proposed to explain the origin of XMR, for example, magnetic field induced metal-to-insulator transition [2], the breaking of topological protection [36], or the compensation of hole and electron [8,14]. For a semimetal with topologically nontrivial electronic structure, the topological protection suppresses backscattering at zero magnetic field. The application of a field will break the protection and result in XMR [36]. However, the nontrivial topological state is not indispensable for the generation of XMR since topologically trivial materials (such as LaSb [4], YSb [17,19], and CeSb [23]) can also exhibit XMR. In fact, XMR can be explained by the electron-hole compensation from the semiclassical two-band model [8,14]. In that case, the balance between electron concentration and hole concentration will lead to unsaturated quadratic behavior of the MR, and the value of MR depends on the mobility of carriers.

The topological property of the LnX family is interesting. A previous theoretical work [1] predicts that LaX (X=N, P, As, Sb, Bi) are topological semimetals or topological insulators. Later ARPES experiments show that LaSb is a topologically trivial material without band inversion [4] while LaBi is a topological semimetal with multiple Dirac cones in the surface band structure [12,15]. By drawing the topological phase diagram of CeX (X=P, As, Sb, Bi) as a function of the spin-orbit-coupling (SOC) effect, Kuroda *et al.* demonstrates the topological phase transition from trivial to nontrivial with the increase of the SOC effect [24]. Consequently, it is of interest to explore the possible topological materials in other members of LnX with strong SOC effect.

TmSb is an isostructural compound to LaSb/LaBi. In this work, we have grown the high quality single crystals of TmSb and investigated the detailed magnetotransport properties and the electronic structure. The transverse MR of TmSb reaches 3.31×10^4% at 2.3 K & 14 T. The split of Fermi surfaces (FSs) is found through the analysis of SdH oscillation, which is attributed to the nonsymmetric spin-orbit interaction. The angle-dependent MR are measured to clarify the contribution of each Fermi surface (FS) to the conductivity. In addition, the electronic structure of TmSb has been studied by ARPES experiments and first-principles calculations. The trivial Berry phase and the absence of band inversion indicate that TmSb is a topologically trivial semimetal. The Hall measurements reveal the compensation of carriers and the high mobility, which constitute the origin of the observed XMR.

II. EXPERIMENTAL METHODS AND CRYSTAL STRUCTURE

Single crystals of TmSb were grown from Sb flux. Tm and excess Sb were placed in a crucible with a ratio of Tm:Sb=1:6. Then the crucible was sealed into an evacuated quartz tube and heated to 1150 °C. After cooling to 750 °C in 300 hours, the excess antimony flux was removed with a centrifuge. The elemental composition was checked by energy

*tlxia@ruc.edu.cn

dispersive x-ray spectroscopy (EDS, Oxford X-Max 50). X-ray diffraction (XRD) patterns of powder and single crystal were collected from a Bruker D8 Advance x-ray diffractometer using Cu K_α radiation. TOPAS-4.2 was employed for the refinement. Resistivity measurements were performed on a Quantum Design physical property measurement system (QD PPMS-14T). ARPES measurements were taken at the Dreamline beamline of the Shanghai Synchrotron Radiation Facility (SSRF). The crystals were cleaved *in situ* along the (*0 0 1*) plane and measured at T $\sim$ 20 K with a working vacuum better than 5×10^{-11} Torr. The first-principles calculations were performed with the projector augmented wave (PAW) method [37,38] as implemented in the VASP package [39]. For the exchange-correlation functional, we adopted the generalized gradient approximation (GGA) of Perdew-Burke-Ernzerhof (PBE) type [40]. The kinetic energy cutoff of the plane-wave basis was set to be 250 eV. The Brillouin zone was sampled with a $20 \times 20 \times 20$ k-point mesh and the Gaussian smearing method with a width of 0.05 eV was used to broaden the Fermi surface. Both cell parameters and internal atomic positions were fully relaxed until all forces became less than 0.01 eV/Å. The calculated lattice constant 6.131 Å of TmSb agrees well with the experimental value 6.105 Å [41]. In the study of electronic structure, the modified Becke-Johnson (MBJ) [42] exchange potential at the meta-GGA level of the Jacobs ladder was used and the SOC effect was included. For the calculations of Fermi surfaces, the maximally localized Wannier functions (MLWF) method [43,44] was employed. TmSb crystallizes in the NaCl-type structure as shown in the inset of Fig. 1(a). The obtained TmSb crystals are in the shape of cubes. The single crystal XRD pattern indicates that the surface of the crystal is the (*0 0 l*) plane [Fig. 1(a)]. The powder XRD pattern of TmSb crystals can be well refined as shown in Fig. 1(b). The refined lattice parameter a(6.08(0)Å) is in good agreement with the value in the Inorganic Crystal Structure Database (ICSD) [41].

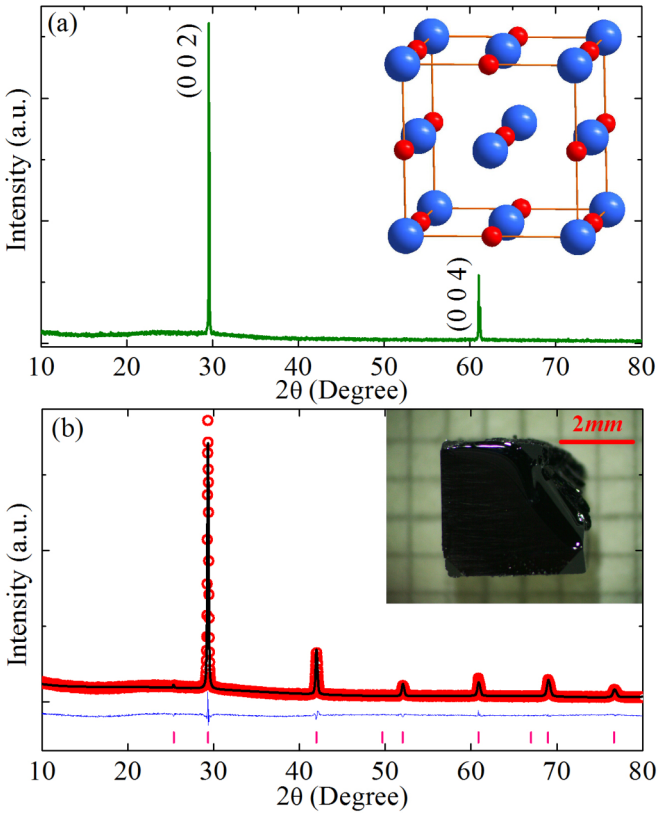

FIG. 1. (a) Single crystal XRD pattern of a TmSb crystal, showing only the (*0 0 l*) reflections. Inset: the crystal structure of TmSb. The blue and red balls represent Tm and Sb, respectively. (b) Powder XRD pattern of TmSb with refinement. Red circle and black solid line represent the data of experiment and the fit curve, respectively. The difference plot is in blue. The pink vertical lines denote the positions of Bragg peaks of TmSb. The inset is an image of TmSb single crystal.

III. RESULTS AND DISCUSSION

We have investigated the magnetotransport properties of TmSb in detail. Figure 2(a) shows the temperature dependent resistivity $\rho_{xx}(T)$ under different magnetic fields. TmSb exhibits metallic behavior under zero magnetic field. After applying a moderate field, an upturn appears in $\rho_{xx}(T)$ curve with the temperature decreased. The upturn can be enhanced by increasing magnetic field. Similar behavior has also been observed in the isostructural compounds LaSb/LaBi/YSb [2,8,9,17] and other XMR materials (such as WTe_2 [28], $NbAs_2/TaAs_2$ [31]). Especially in WTe_2, the upturn has been successfully explained by the following of Kohler's rule in high quality samples with low charge carrier density [29]. Resistivity plateau is another phenomenon usually observed in XMR materials. The resistivity plateau seems to be absent in TmSb. However, as seen in the $\partial\rho/\partial T$ curves [inset on the left of Fig. 2(a)] derived from the main panel, a minimum at $T_i \sim 5.6$ K can be obtained under different fields, indicating that the resistivity plateau starts to emerge. The resistivity plateau is suggested to originate from the temperature-insensitive resistivity at zero field [7,14]. The inset on the right of Fig. 2(a) plots the transverse MR of TmSb as a function of field. The MR follows $B^{1.76}$ (red solid line) and the value reaches 3.31×10^4% at 2.3 K & 14 T. Usually, in semimetals with perfect electron-hole compensation, the MR will exhibit quadratic behavior (MR $\propto B^2$) and not be saturated. The index in TmSb deviates from 2, indicating that the electron and hole in TmSb may be slightly imbalanced.

SdH oscillation has been observed at low temperature and high field [Fig. 2(b)]. The oscillation becomes weaker with the increase of temperature. After subtracting a smooth background, the SdH oscillation amplitude $\Delta\rho_{xx} = \rho_{xx} - \langle\rho_{xx}\rangle$ can be obtained as shown in the inset of Fig. 2(b). Figure 2(c) presents the fast Fourier transform (FFT) analysis of the SdH oscillation. Seven peaks (including three pairs of peaks and one single peak) are identified from the FFT spectra. Since the Onsager relation $F = (\phi_0/2\pi^2)A = (\hbar/2\pi e)A$ describes that the frequency F is proportional to the extremal cross-sectional area A of FS normal to the field, three pairs of peaks mean the FSs split under the field. In fact, the split of FSs has also been observed in de Haas-van Alphen (dHvA) type oscillation of TmSb [45]. TmSb is paramagnetic [46], and the large magnetization is contributed by the local magnetic moment of Tm^{3+} ions which develops with the application of magnetic field [45]. The spin degeneracy is lifted under the field and the

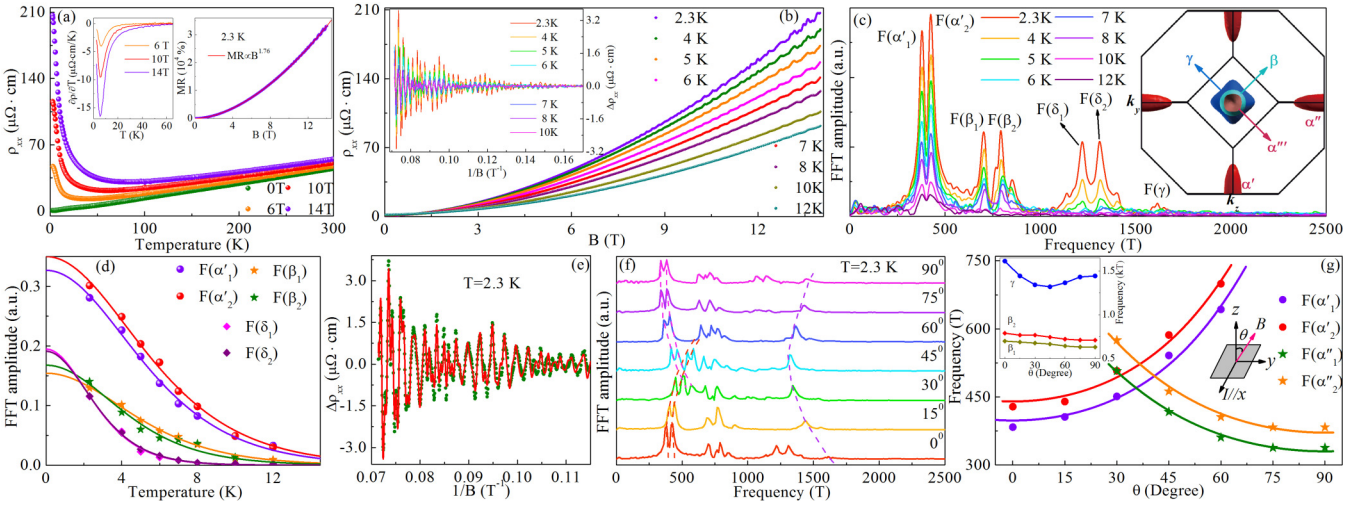

FIG. 2. Magnetotransport properties of TmSb (Sample 1, RRR=70). (a) Temperature dependence of resistivity $\rho_{xx}(T)$ at $B = 0$ T, 6 T, 10 T, 14 T. Inset on the left: $\partial\rho/\partial T$ as a function of temperature. Inset on the right: MR versus magnetic field B at 2.3 K. The MR follows $B^{1.76}$, which can be well fitted as shown in the red solid line. (b) Magnetic field dependence of resistivity $\rho_{xx}(B)$ at different temperatures. Inset: The amplitude of SdH oscillation plotted as a function of 1/B. (c) The FFT spectra of the corresponding oscillations. Inset: The projection of the calculated FSs from the direction of k_x. (d) Temperature dependent FFT amplitude of the frequencies. The solid lines are fittings using the thermal factor in LK formula. (e) The fit (red solid line) of SdH oscillation at 2.3 K using the multiband LK formula. (f) FFT spectra of the SdH oscillations with the change of θ at 2.3 K. (g) The frequencies originating from electronlike FSs plotted as a function of the angle θ. The solid lines are fits to the equation presented in the text. The inset on the left shows angle dependence of the frequencies originating from holelike FSs. The inset on the right is a schematic diagram of the measurements.

nonsymmetric spin-orbit interaction is formed [47], resulting in the split of FSs.

The inset of Fig. 2(c) shows the projection of the calculated FSs on the k_y-k_z plane. In the current measurement ($I//x$, $B//z$), there are three kinds of electronlike FSs (α', α'' and α''') based on the difference of extremal cross-sectional area. The other two holelike FSs are denoted as β and γ, respectively. However, only the frequencies from α', β, and γ are observed in the FFT spectra [F(δ_1) and F(δ_2) come from the mixture of the FSs α' and α'', which will be discussed below]. The absence of the frequencies from α'' and α''' is understandable. Since the field is parallel to the z axis, the extremal cross-sectional area of α'' is close to that of β. So the frequencies from α'' mix with that from β and cannot be separated in the FFT spectra. Rotating the field will change the extremal cross-sectional area of α'' and make its corresponding frequencies appear, which has been proven by the angle-dependent MR (see below). For the elliptical FS α''', a possible explanation is that the mobility along the long axis is much smaller than the mobility along the short axis. Such anisotropic mobility has been derived from the quantitative analysis in YSb/LaSb, where both the anisotropy and multiband nature are considered [7,20].

The amplitude of SdH oscillation is described by Lifshitz-Kosevich (LK) formula:

$$\Delta\rho \propto \frac{\lambda T}{\sinh(\lambda T)} e^{-\lambda T_D} \cos\left[2\pi\left(\frac{F}{B} - \frac{1}{2} + \beta + \delta\right)\right]. \quad (1)$$

In the formula, $\lambda = (2\pi^2 k_B m^*)/(\hbar e B)$. k_B and m^* are the Boltzmann constant and the effective mass of carrier, respectively. T_D is the Dingle temperature, and $2\pi\beta$ is the Berry phase. δ is a phase shift, with the value of $\delta = 0$ and $\pm 1/8$ for the 2D and 3D systems, respectively. Figure 2(d) shows the temperature dependence of FFT amplitude of the corresponding frequencies. The data can be well fitted by the thermal factor $R_T = (\lambda T)/\sinh(\lambda T)$ in LK formula. The fitted effective masses (see Table I) are comparable with that of LaSb [3] and NdSb [25]. As for F(δ_1) and F(δ_2), the effective masses are $0.554m_e$ and $0.542m_e$, respectively. Berry phase is a way to roughly estimate the topological property of the materials. Since the oscillation is multifrequency, we fit the oscillation pattern using multiband LK formula [Fig. 2(e)] to obtain the values of the Berry phase and Dingle temperature. As shown in Table I, the values of Berry phase are far away from the nontrivial value π, suggesting that TmSb is possible topologically trivial material.

Angle-dependent MR measurements are performed to further understand the contribution of each FS. Figure 2(f) shows the FFT spectra of SdH oscillations with rotating the field in the y-z plane. With the θ changing from 0° to 90°, the extremal cross-sectional area of α' normal to the field increases while that of α'' decreases. As a result, the frequencies from α' increases, and the frequencies from

TABLE I. Parameters derived from SdH oscillation. F, oscillation frequency; A, extremal cross-sectional area of FS normal to field; k_F, Fermi vector; m^*, effective mass; T_D, Dingle temperature; $2\pi\beta$, Berry phase.

	F (T)	A (Å^{-2})	k_F (Å^{-1})	m^*/m_e	T_D (K)	$2\pi\beta$
α'_1	383.5	0.037	0.108	0.278	11.4	$0.38\pi + 0.25\pi$
α'_2	428.6	0.041	0.114	0.264	10.5	$-0.27\pi + 0.25\pi$
β_1	699.3	0.067	0.146	0.300	8.5	$0.29\pi - 0.25\pi$
β_2	795.2	0.076	0.155	0.345	5.8	$0.29\pi - 0.25\pi$

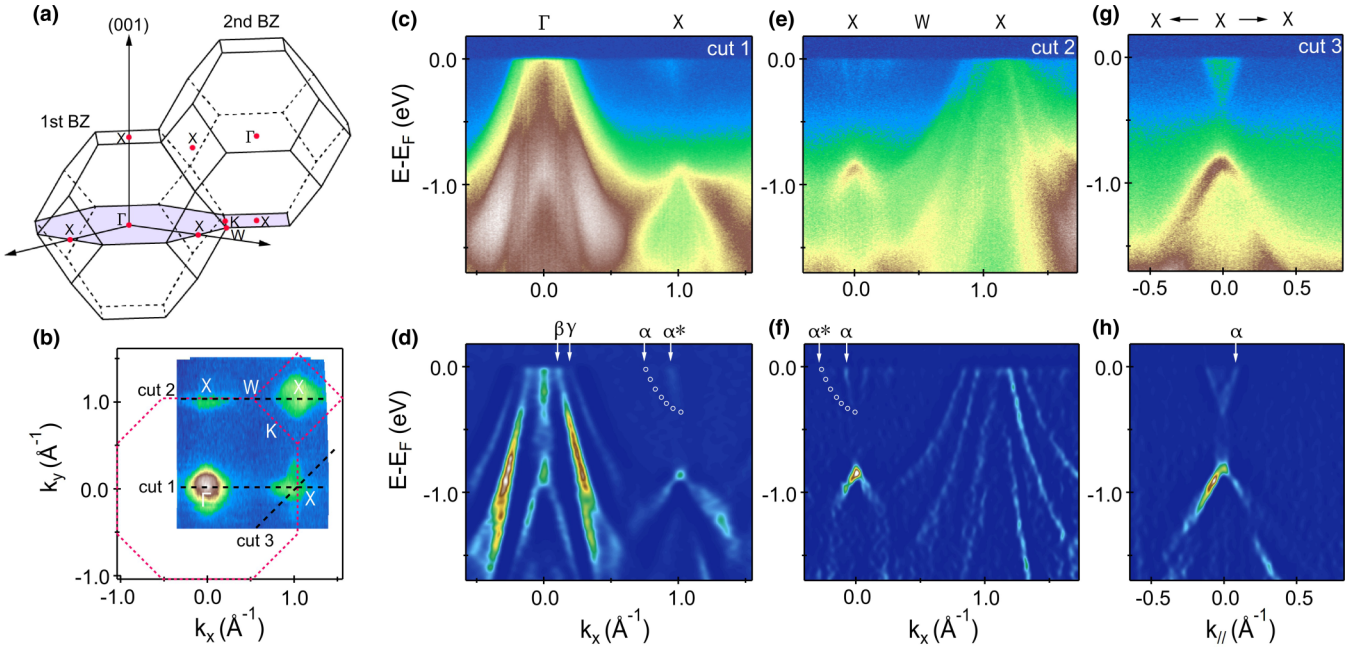

FIG. 3. Fermi surface intensity plot and band dispersions along high-symmetry directions measured by ARPES. (a) Schematic of the first and second 3D BZs with high symmetry points marked by red points. The purple area illustrates the k-space location of the red lines in (b), which indicates the mapping area. (b) ARPES intensity plot of TmSb close to $k_z \sim 0$ with $hv = 53$ eV at T $\sim$ 20 K with high symmetry points marked on it. (c), (e), (g) Photoemission intensity plots of cut1, cut2, and cut3 indicated in (b), respectively. (d), (f), (h) 2D curvature intensity plots of (c), (e), (g), respectively, and white open circles in (d) and (f) indicate half of the larger electron pockets at X points.

α'' can be identified when $\theta = 30^\circ$ before decreasing with angle gradually. The angle-dependent frequencies from β are nearly unchanged while the frequency from γ varies slightly.

Figure 2(g) presents the angle dependence of the frequencies. Two-dimensional FS is suggested to exist in LaSb since the frequency $F(\theta)$ follows $F(0)/\cos(\theta - n\pi/2)$ [2]. However, the data in TmSb can't be well fitted (not presented here) by the above function. In fact, it is suggested to be a pseudo-two-dimensional characteristic of ellipsoidal FS [9], because the extremal cross-sectional area $A = \pi ab/\sqrt{\sin^2\theta + (a^2/b^2)\cos^2\theta}$ (a and b are the semimajor and semiminor axes of the ellipsoid, respectively) can be approximated as $\pi b^2/\cos\theta$ for small θ values and $a \gg b$. Reasonably, the equation $F(\theta) = F(0)/\sqrt{(b/a)^2\sin^2(\theta - n\pi/2) + \cos^2(\theta - n\pi/2)}$ ($n = 0$, 1 for $\alpha_1'(\alpha_2')$, $\alpha_1''(\alpha_2'')$, respectively) is employed to describe the angle-dependent frequencies and the experimental data can be well fitted as shown by the solid lines in Fig. 2(g). The obtained a/b of FS α_1'' (α_2'') is 2.06 (2.07). Then the values of F(α_1'') = 697.0 T and F(α_2'') = 793.8 T at $\theta = 0^\circ$ can be derived, which are close to F(β_1) and F(β_2) as expected. Then the frequency F(δ_1) can be identified as F(α_2') + F(α_2''). Such a frequency is the consequence of magnetic breakdown effect [48], which is caused by quantum tunneling of carriers between the orbits on different FSs [49]. F(δ_2) is the split frequency of F(δ_1) under the field, which has a similar effective mass as F(δ_1). As shown in the inset of Fig. 2(g), with the change of θ, the frequencies from β are nearly unchanged while the frequency from γ varies slightly. Such behaviors are expected since the FS β is nearly spherical and the FS γ is slightly anisotropic. The behavior of angle-dependent frequencies is clearly related to the shape of FSs.

ARPES measurements were performed to reveal the electronic structure of TmSb. TmSb crystalizes in a face-centered cubic (FCC) structure. The first and second three-dimensional Brillouin zones (BZs) are shown in Fig. 3(a). ARPES measurements were performed at T $\sim$ 20 K at a photon energy of 53 eV. Figure 3(b) shows the measured Fermi surface map close to the $k_z \sim 0$ plane, which contains pockets at the Γ and X points. To reveal their dispersions, we show in Figs. 3(c), 3(e) and 3(g) cuts through these pockets as indicated by lines in Fig. 3(b). To enhance the dispersing bands, the corresponding curvature [50] plots are also shown in Figs. 3(d), 3(f) and 3(h). The pockets at the Γ point are clearly identified to be hole pockets and labeled by β and γ in Fig. 3(d). The ellipsoidlike pocket at each X point is labeled by α in Figs. 3(d), 3(f) and 3(h), which is also seen in calculations in Fig. 4(b) with its long axis along the Γ-X direction. We note that there exit two hole pockets in Figs. 3(e) and 3(f) at the X point which are similar to the two hole pockets β and γ at the Γ point in Figs. 3(c) and 3(d). Similar observation has been reported in LaSb [4,15], LaBi [15], and YSb [19]. There are two possible scenarios for explaining this: (1) k_z broadening; (2) band folding due to new surface reconstruction. Because negligible change is observed in the measured dispersion when changing photon energies similar to that reported in LaBi and LaSb [15], we think that k_z broadening is a more likely scenario. This suggests that those in Figs. 3(e) and 3(f) may come from the $k_z \sim 0.5$ plane (top or bottom of the Brillouin zone). The electron pocket labeled with α^* in Figs. 3(d) and 3(f) is also from this k_z broadening. In all the cuts, an energy gap of $\sim$0.5 eV is observed at the X point between the conduction band α and the valence bands. The absence of band anticrossing along the Γ-X direction indicates the topologically trivial characteristic

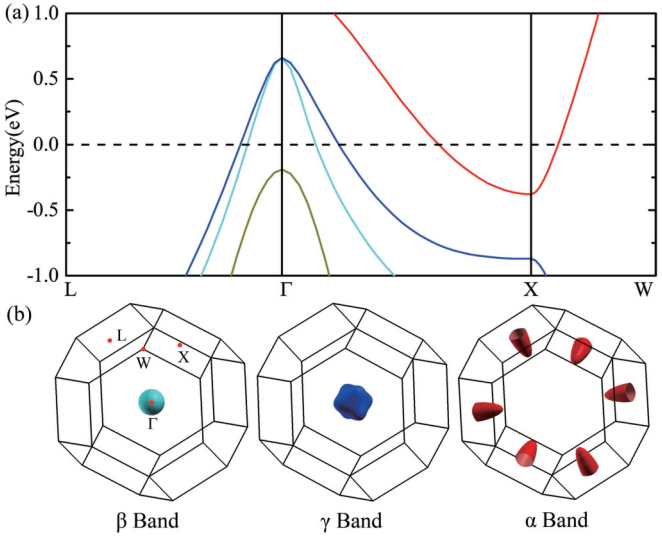

FIG. 4. (a) Band structure along high-symmetry directions of the Brillouin zone and (b) Fermi surfaces of TmSb calculated with the MBJ potential and including the SOC effect. The Fermi level is set to zero.

of TmSb, which is similar to the case of LaSb and YSb [4,17,19].

First-principles calculations have also been employed to study the electronic structure of TmSb. As shown in Fig. 4(a), the calculated band structure is quite consistent with that observed by ARPES. There are two hole bands (β and γ) and one electron band (α) crossing the Fermi level. The gap at the X point is about 0.49 eV. Combined with the trivial Berry phase obtained from SdH oscillation and the electronic structure revealed by ARPES experiments and first-principles calculations, TmSb is suggested to be a topologically trivial semimetal. Figure 4(b) presents the calculated FSs of TmSb with the SOC effect included. The colors of the FSs are in a one-to-one relationship with the corresponding bands crossing the Fermi level. For the two hole pockets, β is nearly spherical, but γ has a FS stretched in the {100} directions. The electron pockets α are ellipsoidal and located at every X point.

Since the topological trivial characteristic of TmSb has been confirmed in the above discussion, the breaking of topological protection is not suitable to explain the origin of XMR in TmSb. Hall measurements are taken to achieve the information about carriers and to reveal the origin of XMR in TmSb. Figure 5(a) shows the field dependence of Hall resistivity $\rho_{xy} = [\rho_{xy}(+B) - \rho_{xy}(-B)]/2$ of TmSb. The ρ_{xy} curves are nonlinear, indicating that the electron and hole coexist in TmSb. The Hall resistivity can be described by the semiclassical two-band model:

$$\rho_{xy} = \frac{B}{e}\frac{\left(n_h\mu_h^2 - n_e\mu_e^2\right) + (n_h - n_e)(\mu_h\mu_e)^2B^2}{(n_h\mu_h + n_e\mu_e)^2 + (n_h - n_e)^2(\mu_h\mu_e)^2B^2}, \quad (2)$$

where $\mu_h(\mu_e)$ and $n_h(n_e)$ are hole (electron) mobility and hole (electron) concentration, respectively. As shown by the red solid lines in Fig. 5(a), the data can be well fitted by the two-band model. Figure 5(b) presents the temperature dependent carriers' concentrations and mobility, which are derived from the fitting. The concentrations at 2.5 K are

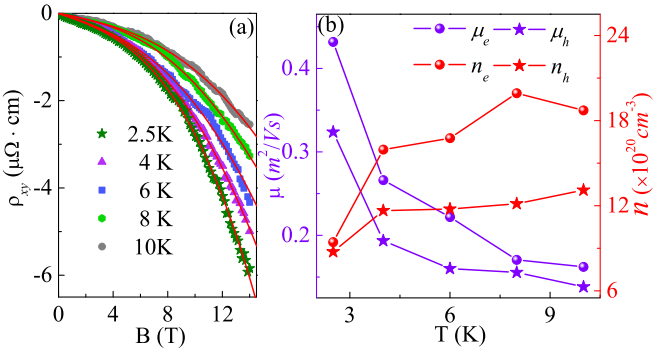

FIG. 5. (a) Magnetic field dependence of Hall resistivity at different temperatures (Sample 2, RRR=24.1, $MR_{2.8K,14T} = 7.62 \times 10^3\%$). The red solid lines are the fits using the two-band model. (b) The obtained carriers concentrations and mobility from the fits.

$n_e = 9.43 \times 10^{20}$ cm^{-3} and $n_h = 8.75 \times 10^{20}$ cm^{-3}. The ratio $n_h/n_e \approx 0.93$ indicates the compensation of hole and electron in TmSb. The values of mobility at 2.5 K ($\mu_e = 4.32 \times 10^3$ cm^2 V^{-1} s^{-1}, $\mu_h = 3.24 \times 10^3$ cm^2 V^{-1} s^{-1}) are lower than those of LaSb/LaBi/YSb [3,8,17], which may be caused by the lower quality of the sample used to measure the Hall resistivity.

In the case of perfect electron-hole compensation ($n_e = n_h$), the relation $MR = \mu_e\mu_h B^2$ can be derived from the field dependent resistivity:

$$\rho(B) = \frac{(n_h\mu_h + n_e\mu_e) + (n_h\mu_e + n_e\mu_h)\mu_h\mu_e B^2}{e(n_h\mu_h + n_e\mu_e)^2 + e(n_h - n_e)^2(\mu_h\mu_e)^2B^2}. \quad (3)$$

Obviously, the MR will be unsaturated, and the value of MR depends on the mobility of carriers. If the compensation is imperfect, the MR can be expressed as follows,

$$MR = \frac{\eta(\mu_h + \mu_e)^2\mu_h\mu_e B^2}{(\eta\mu_h + \mu_e)^2 + (\eta - 1)^2(\mu_h\mu_e)^2B^2}, \quad (4)$$

where $\eta = n_h/n_e$ ($\eta \neq 1$ but close to 1). The MR will deviate from quadratic behavior slightly, and the feature of unsaturation retains when the value of $(\eta - 1)$ is small. In TmSb, the compensated carrier concentrations and high mobility are suggested to be responsible for the XMR. Even the ratio $\eta \approx 0.93$ indicates that the compensation is not very perfect, the MR is still unsaturated and deviates from quadratic behavior slightly as expected.

IV. SUMMARY

In summary, single crystals of TmSb are grown and the magnetotransport properties have been investigated. Analysis on the FFT spectra of the SdH oscillations observed at low temperature and high field clearly indicates the split of Fermi surfaces. The extracted trivial Berry phase from the fit of LK formula, combining with the electronic structures from ARPES measurements and first-principles calculations confirm that TmSb is a semimetal with topologically trivial band structures and nearly compensated concentrations of electron and hole. The XMR in TmSb is attributed to the electron-hole compensation and high mobility of carriers.

ACKNOWLEDGMENTS

We thank Peng-Jie Guo for helpful discussions. This work is supported by the National Natural Science Foundation of China (Grants No. 11574391, No. 11774424, No. 11474356, and No. 91421304), the Fundamental Research Funds for the Central Universities, and the Research Funds of Renmin University of China (Grants No. 14XNLQ07, No. 14XNLQ03, and No. 16XNLQ01). Computational resources have been provided by the Physical Laboratory of High Performance Computing at Renmin University of China. The Fermi surfaces were prepared with the XCRYSDEN program [51].

[1] M. Zeng, C. Fang, G. Chang, Y.-A. Chen, T. Hsieh, A. Bansil, H. Lin, and L. Fu, arXiv:1504.03492.
[2] F. F. Tafti, Q. D. Gibson, S. K. Kushwaha, N. Haldolaarachchige, and R. J. Cava, Nat. Phys. **12**, 272 (2016).
[3] F. F. Tafti, Q. Gibson, S. Kushwaha, J. W. Krizan, N. Haldolaarachchige, and R. J. Cava, Proc. Natl. Acad. Sci. USA **113**, E3475 (2016).
[4] L.-K. Zeng, R. Lou, D.-S. Wu, Q. N. Xu, P.-J. Guo, L.-Y. Kong, Y.-G. Zhong, J.-Z. Ma, B.-B. Fu, P. Richard, P. Wang, G. T. Liu, L. Lu, Y.-B. Huang, C. Fang, S.-S. Sun, Q. Wang, L. Wang, Y.-G. Shi, H. M. Weng, H.-C. Lei, K. Liu, S.-C. Wang, T. Qian, J.-L. Luo, and H. Ding, Phys. Rev. Lett. **117**, 127204 (2016).
[5] W.-J. Ban, W.-T. Guo, J.-L. Luo, and N.-L. Wang, Chin. Phys. Lett. **34**, 077804 (2017).
[6] P.-J. Guo, H.-C. Yang, K. Liu, and Z.-Y. Lu, Phys. Rev. B **96**, 081112 (2017).
[7] F. Han, J. Xu, A. S. Botana, Z. L. Xiao, Y. L. Wang, W. G. Yang, D. Y. Chung, M. G. Kanatzidis, M. R. Norman, G. W. Crabtree, and W. K. Kwok, Phys. Rev. B **96**, 125112 (2017).
[8] S. Sun, Q. Wang, P.-J. Guo, K. Liu, and H. Lei, New J. Phys. **18**, 082002 (2016).
[9] N. Kumar, C. Shekhar, S.-C. Wu, I. Leermakers, O. Young, U. Zeitler, B. Yan, and C. Felser, Phys. Rev. B **93**, 241106 (2016).
[10] Y. Wu, T. Kong, L.-L. Wang, D. D. Johnson, D. Mou, L. Huang, B. Schrunk, S. L. Bud'ko, P. C. Canfield, and A. Kaminski, Phys. Rev. B **94**, 081108 (2016).
[11] R. Lou, B.-B. Fu, Q. N. Xu, P.-J. Guo, L.-Y. Kong, L.-K. Zeng, J.-Z. Ma, P. Richard, C. Fang, Y.-B. Huang, S.-S. Sun, Q. Wang, L. Wang, Y.-G. Shi, H. C. Lei, K. Liu, H. M. Weng, T. Qian, H. Ding, and S.-C. Wang, Phys. Rev. B **95**, 115140 (2017).
[12] J. Nayak, S.-C. Wu, N. Kumar, C. Shekhar, S. Singh, J. Fink, E. E. Rienks, G. H. Fecher, S. S. Parkin, B. Yan *et al.*, Nat. Commun. **8**, 13942 (2017).
[13] R. Singha, B. Satpati, and P. Mandal, Sci. Rep. **7**, 6321 (2017).
[14] P.-J. Guo, H.-C. Yang, B.-J. Zhang, K. Liu, and Z.-Y. Lu, Phys. Rev. B **93**, 235142 (2016).
[15] X. H. Niu, D. F. Xu, Y. H. Bai, Q. Song, X. P. Shen, B. P. Xie, Z. Sun, Y. B. Huang, D. C. Peets, and D. L. Feng, Phys. Rev. B **94**, 165163 (2016).
[16] N. Ghimire, A. Botana, D. Phelan, H. Zheng, and J. Mitchell, J. Phys.: Condens. Matter **28**, 235601 (2016).
[17] Q.-H. Yu, Y.-Y. Wang, R. Lou, P.-J. Guo, S. Xu, K. Liu, S. Wang, and T.-L. Xia, EPL **119**, 17002 (2017).
[18] O. Pavlosiuk, P. Swatek, and P. Wiśniewski, Sci. Rep. **6**, 38691 (2016).
[19] J. He, C. Zhang, N. J. Ghimire, T. Liang, C. Jia, J. Jiang, S. Tang, S. Chen, Y. He, S.-K. Mo, C. C. Hwang, M. Hashimoto, D. H. Lu, B. Moritz, T. P. Devereaux, Y. L. Chen, J. F. Mitchell, and Z.-X. Shen, Phys. Rev. Lett. **117**, 267201 (2016).
[20] J. Xu, N. J. Ghimire, J. S. Jiang, Z. L. Xiao, A. S. Botana, Y. L. Wang, Y. Hao, J. E. Pearson, and W. K. Kwok, Phys. Rev. B **96**, 075159 (2017).
[21] N. Alidoust, A. Alexandradinata, S.-Y. Xu, I. Belopolski, S. K. Kushwaha, M. Zeng, M. Neupane, G. Bian, C. Liu, D. S. Sanchez *et al.*, arXiv:1604.08571.
[22] L. Ye, T. Suzuki, C. R. Wicker, and J. G. Checkelsky, arXiv:1704.04226.
[23] H. Oinuma, S. Souma, D. Takane, T. Nakamura, K. Nakayama, T. Mitsuhashi, K. Horiba, H. Kumigashira, M. Yoshida, A. Ochiai, T. Takahashi, and T. Sato, Phys. Rev. B **96**, 041120 (2017).
[24] K. Kuroda, M. Ochi, H. Suzuki, M. Hirayama, M. Nakayama, R. Noguchi, C. Bareille, S. Akebi, S. Kunisada, T. Muro *et al.*, arXiv:1707.06500.
[25] N. Wakeham, E. D. Bauer, M. Neupane, and F. Ronning, Phys. Rev. B **93**, 205152 (2016).
[26] M. Neupane, M. M. Hosen, I. Belopolski, N. Wakeham, K. Dimitri, N. Dhakal, J.-X. Zhu, M. Z. Hasan, E. D. Bauer, and F. Ronning, J. Phys.: Condes. Matter **28**, 23LT02 (2016).
[27] Y. Wu, Y. Lee, T. Kong, D. Mou, R. Jiang, L. Huang, S. L. Bud'ko, P. C. Canfield, and A. Kaminski, Phys. Rev. B **96**, 035134 (2017).
[28] M. N. Ali, J. Xiong, S. Flynn, J. Tao, Q. D. Gibson, L. M. Schoop, T. Liang, N. Haldolaarachchige, M. Hirschberger, N. P. Ong, and R. J. Cava, Nature (London) **514**, 205 (2014).
[29] Y. L. Wang, L. R. Thoutam, Z. L. Xiao, J. Hu, S. Das, Z. Q. Mao, J. Wei, R. Divan, A. Luican-Mayer, G. W. Crabtree, and W. K. Kwok, Phys. Rev. B **92**, 180402 (2015).
[30] J. Jiang, F. Tang, X. C. Pan, H. M. Liu, X. H. Niu, Y. X. Wang, D. F. Xu, H. F. Yang, B. P. Xie, F. Q. Song, P. Dudin, T. K. Kim, M. Hoesch, P. K. Das, I. Vobornik, X. G. Wan, and D. L. Feng, Phys. Rev. Lett. **115**, 166601 (2015).
[31] Y.-Y. Wang, Q.-H. Yu, P.-J. Guo, K. Liu, and T.-L. Xia, Phys. Rev. B **94**, 041103 (2016).
[32] Z. Yuan, H. Lu, Y. Liu, J. Wang, and S. Jia, Phys. Rev. B **93**, 184405 (2016).
[33] D. Wu, J. Liao, W. Yi, X. Wang, P. Li, H. Weng, Y. Shi, Y. Li, J. Luo, X. Dai *et al.*, Appl. Phys. Lett. **108**, 042105 (2016).
[34] Y. Luo, R. McDonald, P. Rosa, B. Scott, N. Wakeham, N. Ghimire, E. Bauer, J. Thompson, and F. Ronning, Sci. Rep. **6**, 27294 (2016).
[35] B. Shen, X. Deng, G. Kotliar, and N. Ni, Phys. Rev. B **93**, 195119 (2016).
[36] T. Liang, Q. Gibson, M. N. Ali, M. Liu, R. Cava, and N. Ong, Nat. Mater. **14**, 280 (2015).
[37] P. E. Blöchl, Phys. Rev. B **50**, 17953 (1994).
[38] G. Kresse and D. Joubert, Phys. Rev. B **59**, 1758 (1999).
[39] G. Kresse and J. Hafner, Phys. Rev. B **47**, 558 (1993); G. Kresse and J. Furthmüller, Comput. Mater. Sci. **6**, 15 (1996); Phys. Rev. B **54**, 11169 (1996).

[40] J. P. Perdew, K. Burke, and M. Ernzerhof, Phys. Rev. Lett. **77**, 3865 (1996).
[41] M. Abdusalyamova, A. Chuiko, A. Y. Golubkov, S. Popov, L. Parfenova, A. Procofev, and I. Smirnov, J. Alloy. Compd. **205**, 107 (1994).
[42] A. D. Becke and E. R. Johnson, J. Chem. Phys. **124**, 221101 (2006); F. Tran and P. Blaha, Phys. Rev. Lett. **102**, 226401 (2009).
[43] N. Marzari and D. Vanderbilt, Phys. Rev. B **56**, 12847 (1997).
[44] I. Souza, N. Marzari, and D. Vanderbilt, Phys. Rev. B **65**, 035109 (2001).
[45] S. Nimori, G. Kido, D. Li, and T. Suzuki, Physica B (Amsterdam) **211**, 148 (1995).
[46] B. R. Cooper and O. Vogt, Phys. Rev. B **1**, 1211 (1970).
[47] Y. Ōnuki, A. Nakamura, T. Uejo, A. Teruya, M. Hedo, T. Nakama, F. Honda, and H. Harima, J. Phys. Soc. Jpn. **83**, 061018 (2014).
[48] K. Kishigi, M. Nakano, K. Machida, and Y. Hori, J. Phys. Soc. Jpn. **64**, 3043 (1995).
[49] J. Hu, Y. L. Zhu, D. Graf, Z. J. Tang, J. Y. Liu, and Z. Q. Mao, Phys. Rev. B **95**, 205134 (2017).
[50] P. Zhang, P. Richard, T. Qian, Y.-M. Xu, X. Dai, and H. Ding, Rev. Sci. Instrum. **82**, 043712 (2011).
[51] A. Kokalj, Comput. Mater. Sci. **28**, 155 (2003).